

Crossmark

PAPER

RECEIVED
dd Month yyyyREVISED
dd Month yyyy

Substrate-controlled nucleation and growth kinetics in ultrathin Bi₂Te₃ films

Damian Brzozowski¹, Sander R. Hønnås¹, Egil Y. Tokle¹, Jørgen A. Arnesen¹ and Ingrid G. Hallsteinsen^{1,*}

¹Department of Materials Science and Engineering, Norwegian University of Science and Technology, Trondheim, Norway

*Author to whom any correspondence should be addressed.

E-mail: ingrid.hallsteinsen@ntnu.no

Keywords: Bi₂Te₃, nucleation, pulsed laser deposition

Abstract

Metal chalcogenides are promising layered topological materials, yet their electronic performance is often limited by parasitic bulk conduction arising from defects that introduce excess carriers and shift the Fermi level out of the topological regime. Controlling early-stage growth and defect formation is therefore essential for suppressing bulk transport and enhancing surface-state conduction. Here we investigate ultrathin Bi₂Te₃ films grown by pulsed laser deposition on substrates spanning van der Waals, lattice-matched, and amorphous regimes to determine how substrate-dependent nucleation pathways influence defect formation and electronic transport.

Phase-pure, *c*-axis-oriented Bi₂Te₃ forms on all substrates, but the growth morphology varies strongly. Layered growth with well-defined quintuple-layer terraces is governed primarily by substrate roughness rather than lattice match: atomically smooth mica and step-terraced SrTiO₃ yield continuous terraces, whereas rougher BaF₂ and amorphous Si₃N₄ produce island-structured films. Between the two smooth substrates, the higher surface energy of SrTiO₃ enhances adatom adsorption and nucleation density, promoting rapid vertical growth and early Te depletion.

Transport measurements reveal n-type conduction with carrier densities of 10¹⁹–10²⁰ cm⁻³. The highest carrier density occurs for films on SrTiO₃, consistent with defect formation during high-density nucleation, whereas mobility correlates with structural coherence and terrace formation. Weak anti-localization signatures confirm phase-coherent transport in films on mica and SrTiO₃. These results show that substrate roughness and nucleation density provide key levers for controlling defect formation and strengthening topological surface transport in Bi₂Te₃ thin films.

1 Introduction

Bismuth telluride (Bi₂Te₃) is a layered van der Waals material with a narrow band gap of 0.15 eV and strong spin-orbit coupling. The strong spin-orbit coupling leads to a band inversion between the valence band maximum and the conduction band minimum, giving rise to a topological insulator phase [1]. In this state the bulk remains insulating while metallic surface states emerge that are protected by time-reversal symmetry. These spin-momentum-locked surface states have attracted considerable interest for electronic and spintronic application that rely on robust surface transport [2, 3]. In practice, however, electron transport in Bi₂Te₃ is often dominated by bulk conduction due to unintentional defects that introduce excess carriers and shift the Fermi level away from the Dirac point. Achieving surface-dominated transport therefore requires precise control over structural and chemical defects that arise during film growth.

Thin films of Bi₂Te₃ have been realized using a range of deposition techniques, including molecular beam epitaxy (MBE) [4, 5], pulsed laser deposition (PLD) [6, 7], sputtering [8, 9], and physical vapor transport (PVT) [10]. Under optimized conditions these methods typically yield films with strong out-of-plane orientation along the (003*n*) crystallographic planes [11, 12, 13]. These planes correspond to stacks of quintuple layers (QLs) consisting of alternating tellurium and

bismuth atomic planes separated by van der Waals gaps. Although such preferential orientation is commonly observed for films ranging from tens of nanometers to micrometers in thickness, the earliest stages of growth can vary significantly in crystalline quality and stoichiometry [14].

The interaction between the film and the substrate plays a critical role during these initial growth stages. In ideal van der Waals (vdW) epitaxy, layered materials grow on dangling-bond-free surfaces such as mica with minimal lattice constraints. However, when deposited on conventional three-dimensional substrates the interface often exhibits quasi-van der Waals (qvW) epitaxy, where electrostatic or chemical interactions supplement vdW forces. These interactions influence adatom adsorption, surface diffusion, and nucleation density, thereby affecting terrace formation, grain size, and film morphology [15, 16]. Surface roughness and substrate termination further modify these processes by introducing additional nucleation sites and altering local bonding environments.

Defects formed during growth strongly influence the resulting electronic properties. Native point defects such as vacancies, antisite defects, and interstitials modify the carrier concentration and shift the Fermi level into bulk bands, thereby suppressing the contribution from topological surface states [17, 18, 19]. Structural imperfections such as grain boundaries, mosaicity, and dislocations can also affect electron transport by introducing scattering centers and disrupting crystalline coherence. Transport measurements of Bi_2Te_3 films therefore often exhibit contributions from multiple conduction channels. Topological surface states are commonly identified through weak anti-localization (WAL) signatures at low magnetic fields and temperatures. However, WAL may also arise from strong spin-orbit coupling in bulk channels, making it challenging to distinguish surface-related transport from bulk conduction.

Despite extensive studies of Bi_2Te_3 thin films, the relationship between substrate-dependent nucleation processes, structural defects, and electronic transport remains incompletely understood. In particular, it is unclear how differences in substrate roughness, bonding environment, and lattice compatibility influence the early stages of film growth and the resulting transport properties.

In this work, we investigate ultrathin Bi_2Te_3 films deposited on a set of substrates representing distinct epitaxial environments: muscovite mica enabling vdW epitaxy, (111)-oriented BaF_2 providing near lattice matching, (111)-oriented SrTiO_3 representing a qvW interface, and amorphous Si_3N_4 on Si as a non-crystalline surface. By combining structural characterization with electronic transport measurements, we examine how substrate-dependent nucleation and growth pathways influence film morphology, defect formation, and electronic transport in ultrathin Bi_2Te_3 . By systematically comparing these different epitaxial environments, this work aims to clarify how substrate roughness, adsorption strength, and lattice compatibility collectively govern the early stages of growth and the resulting electronic behavior. Establishing these relationships provides insight into how growth kinetics shape defect populations and transport properties in layered topological materials, offering guidelines for optimizing thin-film heterostructures for thermoelectric and quantum electronic applications.

2 Method

Prior to thin film deposition, each substrate was prepared following dedicated protocols. As-received Si_3N_4 substrates (WaferPro) were rinsed in acetone and ethanol. SrTiO_3 substrates (Shinkosha) were etched in a buffered hydrofluoric acid solution (1:9 volumetric ratio of 48% HF and 40% NH_4F) for 45 seconds to ensure titanium single termination and annealed at 1050 °C for 1 hour in an oxygen flow to achieve step terrace surface topography. BaF_2 substrates were annealed at 850 °C for 4 hours in a nitrogen environment. Mica substrates (Agar Scientific) were freshly cleaved with scotch tape prior to deposition to obtain an atomically flat surface.

A KrF excimer laser with wavelength $\lambda = 248$ nm was used to ablate a stoichiometric Bi_2Te_3 target (Kurt J. Lesker, 99.999%). The target-substrate distance was 50 mm. The PLD chamber remained at a background pressure of 2×10^{-8} mbar before introducing argon gas with a working pressure of 1 mbar. The substrate temperature was measured with an external pyrometer and set at 220 °C. To minimize deposition growth rate and promote high quality out-of-plane ordering, laser repetition rate was set to 0.2 Hz, and laser fluence to 0.5 J cm^{-2} . For all substrates, the thickness of the films and the degree of substrate coverage were tuned by changing the number of laser pulses between 10, 25, and 50. Additionally, 1-pulse films were prepared on mica and SrTiO_3 substrates.

After deposition, the Bi_2Te_3 films were cooled naturally to room temperature in the chamber.

Atomic force microscopy was performed in a Bruker Dimension Icon to analyze the roughness of the films and the degree of surface coverage as a function of laser pulses. The probe used was a ScanAsyst-Air with a nominal tip radius of 2 nm. The Gwyddion software [20] was used to estimate surface coverage by marking grains by level threshold. Root mean square roughness values were taken on selected topmost layers of deposited films. Crystalline quality was evaluated with Bragg-Brentano X-ray diffraction using Bruker D8 Discover equipped in the copper source ($K\alpha$ $\lambda = 1.5406 \text{ \AA}$) and (220)-Ge monochromator. The same system was used to perform X-ray reflectivity to evaluate the thickness of the films. X-ray reflectivity data fitting was performed using the Reflex software and based on the Nelder-Mead simplex algorithm [21]. To confirm proper stoichiometry transfer, Raman spectroscopy was employed. The Renishaw InVia Reflex Spectrometer was operating with the grating of 2400 g mm^{-1} , the laser wavelength of 532 nm, and the laser power of 1 mW to prevent surface damage. The signal was averaged over 60 one-second scans.

Magnetoresistance measurements were performed using an attoDRY1000 top-loading pulse tube system with superconducting magnet cryostat. A Keithley 2450 source measure unit, connected to an atto3DR through an ACC100 carrier, was utilized to source currents and measure voltages. Samples were electrically connected through wire bonding with a TPT HB05 Wedge and Ball Bonder in ball/wedge mode, and using silver paint as a conductive adhesive.

For Hall measurements, a current of $10 \mu\text{A}$ was applied between two opposite contacts, and the voltage was measured across the remaining pair in the van der Pauw configuration. Weak anti-localization measurements were performed in a standard van der Pauw geometry, with the current sourced between neighboring contacts and the voltage measured across the remaining pair. An external magnetic field was swept symmetrically around zero field between -1 T and 1 T . Measurements were performed for both sweep directions and current polarities to suppress thermoelectric offsets and residual Hall contributions. To analyze weak anti-localization, low-field magnetoresistance curves were recorded at temperatures between 5 K and 50 K . The weak anti-localization features were fitted using the Hikami-Larkin-Nagaoka model to extract the α prefactor and the phase-coherence length l_ϕ .

3 Results

3.1 Substrate-dependent growth and morphology of Bi_2Te_3

To investigate the early stages of film growth, a thickness series corresponding to 10, 25, and 50 laser pulses was deposited on all four substrates. In addition, 1-pulse films were prepared on mica and SrTiO_3 to probe the earliest nucleation stages. All other deposition parameters were kept constant.

3.1.1 Phase formation and stoichiometry. Raman spectroscopy was used to verify the stoichiometry of the deposited films through their characteristic vibrational modes [10]. The Raman spectra of the films are shown in Figure 1. For the 50-pulse films (yellow lines), peaks are observed at Raman shifts of 62, 103, and approximately 135 cm^{-1} , corresponding to the A_{1g}^1 , E_g^2 and A_{1g}^2 vibrational modes of Bi_2Te_3 . The presence of these modes confirms that the deposited films retain the characteristic 2:3 stoichiometry during laser ablation and adsorption [10, 22, 23, 24].

The Raman intensity decreases for the 25- and 10-pulse (purple and blue lines), consistent with the reduced thickness of these samples. In addition, the A_{1g}^2 mode shifts from approximately 133 cm^{-1} for the 50-pulse films to about 135 cm^{-1} and 138 cm^{-1} for the 25- and 10-pulse films, respectively. This shift is attributed to phonon confinement effects that become increasingly pronounced in ultrathin Bi_2Te_3 layers, consistent with previous reports for discontinuous films composed of isolated grains [25]. In addition, the relative ratio of E_g^2 to A_{1g}^1 is reduced with decreasing thickness, which is a result of the alleviated constraining of the out-of-plane A_{1g} phonon modes in thinner films [26]. The calculated intensity ratios are provided in the Supporting Information.

For the 10-pulse film deposited on SrTiO_3 , the characteristic Bi_2Te_3 Raman modes are absent and replaced by a broad feature around 80 cm^{-1} . Such a signal has been associated with

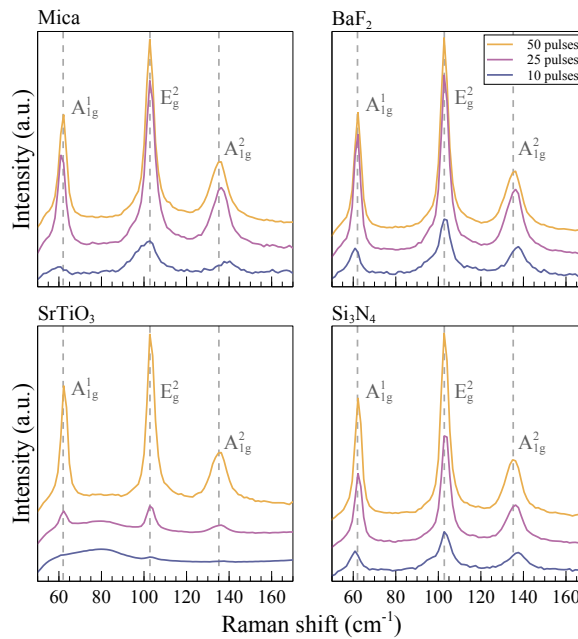


Figure 1: Raman spectra of deposited films. Dashed lines indicate characteristic phonon modes of Bi_2Te_3 .

tellurium-deficient phases such as BiTe and Bi_4Te_3 [10]. This behavior may arise from selective absorption or desorption of Bi and Te adatoms on the polar SrTiO_3 (111) surface during the earliest growth stage. As the film thickness increases, the characteristic Bi_2Te_3 modes reappear, indicating that stoichiometric growth is restored.

3.1.2 Crystallographic orientation and growth rate. X-ray diffraction (XRD) and X-ray reflectivity (XRR) were used to examine the crystallographic orientation and thickness of the films. Widescan Bragg-Brentano diffractograms of the 50-pulse samples are shown in Figure 2(a). Additional diffractograms of the 25- and 10-pulse samples are included in the Supporting Information. All films exhibit reflections at 2θ values corresponding to the (006), (0015) and (0018) lattice planes as marked with the dashed lines. No additional reflections are observed, indicating that the films grow with a strong out-of-plane preferential orientation along the (003*n*) family of planes regardless of substrate type.

XRR measurements reveal substantial differences in film thickness for samples deposited with the same number of laser pulses, as shown in Figure 2(b). For example, the films grown with 50 pulses on mica reaches a thickness of approximately 8 nm, whereas the corresponding film on SrTiO_3 reaches approximately 16 nm. Similar differences are observed for the 25- and 10-pulse films. The 10-pulse film on SrTiO_3 already reaches a thickness of about 7 nm, indicating rapid out-of-plane growth. In contrast, films on Si_3N_4 and BaF_2 reach only 4 nm. On mica, the growth is significantly slower in the vertical direction, reaching only about 1 nm after 10 pulses - atomic force microscopy (AFM) scans included in the Supporting Information confirm these thickness estimations.

3.1.3 Surface morphology. The surface morphology of the 50-pulse films was examined using AFM, as shown in Figure 3. The film grown on mica, Figure 3(a), exhibits a layered morphology with well-defined terraces corresponding to individual QLs. The surface coverage reaches approximately 98%, resulting in a nearly continuous film with low porosity. Triangular grains with two in-plane orientations rotated by 60° are observed in the upper layer, with an average grain size of approximately 100 nm. The lower film layer does not show clear grain boundaries, indicating that the grains are in-plane compatible and eventually coalesce. Step-like features and triangular grains are indicative of the high-quality layer-by-layer deposition [27, 28]. The root-mean-square (RMS) roughness is 0.7 nm, and the extracted step height between adjacent terraces, Figure 3(e), is

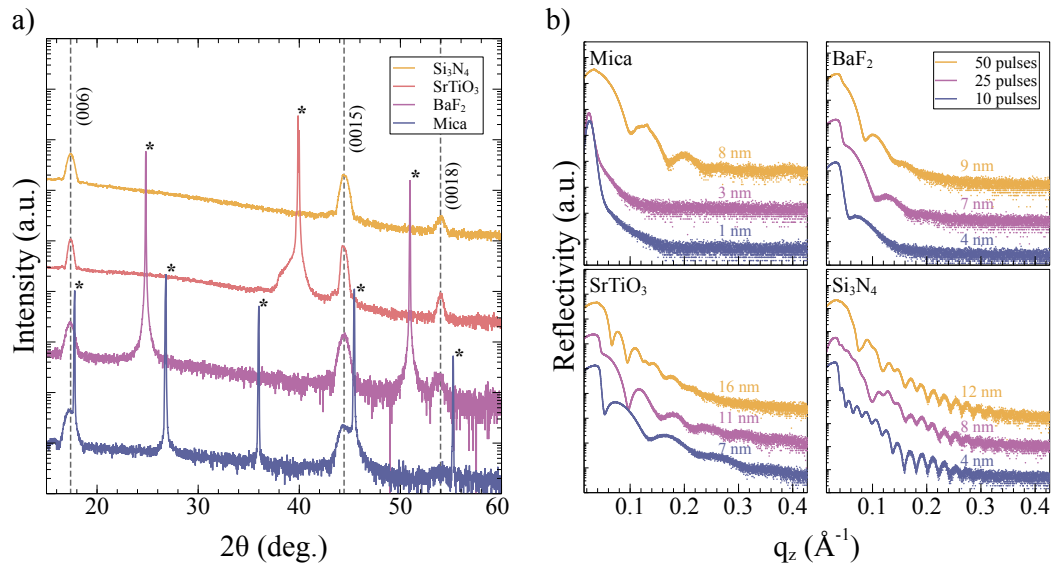


Figure 2: a) XRD wide-scans of the 50 pulse samples, plotted in logarithmic scale. Substrate peaks marked with asterisks. The dashed lines mark $(003n)$ peaks of Bi_2Te_3 . b) XRR profiles of the samples. The profiles were used to estimate sample's thickness. The film grown on Si_3N_4 displays additional, high-frequent reflectivity curves from the $\text{Si}_3\text{N}_4/\text{Si}$ interface

approximately 1 nm, consistent with the thickness of a single QL.

The film grown on SrTiO_3 , Figure 3(c), also exhibits a layered morphology with low roughness (RMS 1.3 nm) and high surface coverage of approximately 95%. However, the grains are smaller, typically 50 nm to 80 nm in size, and multiple stacked layers are visible, indicating a stronger contribution from out-of-plane growth compared to the mica substrate. The height profile shown in Figure 3(g) is not as well defined as that of the mica-based film. However, the step height corresponds closely to the height of 1 QL.

In contrast, films deposited on BaF_2 and Si_3N_4 , Figure 3(b,d), display a markedly different morphology, which is reflected in irregular height profiles plotted in Figure 3(f,h). Instead of well-defined terraces, these films form coalesced networks with irregular grain boundaries and higher porosity. The RMS roughness is significantly larger, particularly for Si_3N_4 , where values of up to 3.4 nm are observed. The scans show no clear separation between the out-of-plane layers or in-plane alignment. The grain sizes range from 100 nm to 200 nm.

Additional comparison of the surface coverage is continued based on the scanning electron microscopy (SEM) images of the 10-pulse films. The images are used to extract the coverage percentage and are included in the Supporting Information. As the thickness decreases and films become progressively less continuous, isolated grain features become dominant on all substrates. The surface coverage of the 10-pulse films varies significantly depending on the substrate type. The film grown on SrTiO_3 reaches approximately 87% coverage, whereas the coverage is about 80% on mica, 76% on BaF_2 , and approximately 60% on Si_3N_4 . This is indicative of a changed deposition rate relative to the 50-pulse films, where the mica-based film yields the highest coverage.

3.1.4 Role of substrate surface properties. The observed differences in film morphology can be related to the surface characteristics of the substrates. Supplementary AFM measurements of the bare substrates show that amorphous Si_3N_4 possesses the highest surface roughness. Both BaF_2 and SrTiO_3 exhibit step-terraced surfaces, although the step-edges of BaF_2 contain protruding particulates that are absent on SrTiO_3 . In contrast, freshly cleaved mica provides an atomically flat surface. These variations in surface morphology strongly influence the early stages of film growth. Films grown the smoother substrates (mica and SrTiO_3) develop layered morphologies with relatively uniform grain distributions, whereas films grown on the rougher substrates (BaF_2 and Si_3N_4) form disordered networks with higher roughness and reduced terrace formation. This comparison indicates that substrate roughness plays a critical role in determining the growth

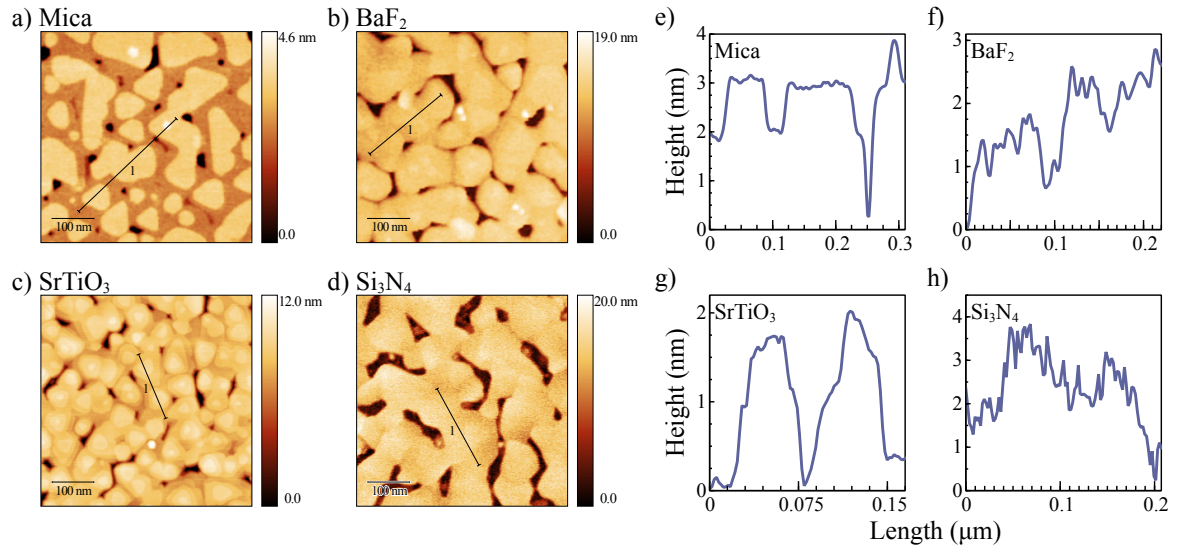


Figure 3: Left panel: 500×500 nm AFM scans of 50 pulse samples. Right panel: height profiles extracted from AFM scans.

kinetics and morphology of ultrathin Bi₂Te₃ films during the early stages of deposition.

3.2 Nucleation

To further probe the earlier stages of film formation, 1-pulse depositions of Bi₂Te₃ were performed on mica and SrTiO₃. Nucleation analysis was not carried out on BaF₂ and Si₃N₄. As discussed in the previous section, both substrates exhibit substantial surface roughness at the nanometer scale, which makes it difficult to reliably distinguish newly formed nuclei from the underlying topography in AFM scans. In contrast, mica provides an atomically flat surface upon cleavage, while SrTiO₃ exhibits well-defined step-terrace structures. These smoother surfaces enable reliable identification of individual nuclei and therefore allow a quantitative analysis of nucleation density.

Figure 4 shows AFM images of the 1-pulse samples on mica and SrTiO₃. On SrTiO₃, the surface is populated by small grains with lateral dimensions of approximately 5 nm to 10 nm. AFM line profiles indicate heights between 2 nm to 3 nm, corresponding to roughly three QLs. The resulting surface coverage is approximately 55%. In contrast, the film grown on mica exhibits significantly lower coverage of about 25%, with islands of approximately 1 nm height corresponding to a single QL. These values translate into a substantial difference in the amount of adsorbed material per area, corresponding to approximately 10 formula units per nm² on SrTiO₃ and about 1.5 formula units per nm² on mica. Because both samples were deposited under identical conditions and therefore experience identical plume dynamics, the observed differences arise from the interaction between incoming species and the substrate surface. The reduced adsorption on mica is consistent with the nature of vdW substrates, which lack dangling bonds and therefore interact only weakly with incoming adatoms. In contrast, the SrTiO₃ surface exposes partially charged and chemically active terminations that provide stronger adsorption sites.

To quantify the nucleation process, we employ the framework described by Mortelmans *et al.* for layered dichalcogenides [29]. Their work established a relationship between nucleation density and defect formation during layered material growth. In particular, higher nucleation densities are often associated with increased densities of structural defects such as grain boundaries and stacking faults. The model also allows comparison of nucleation densities across different growth techniques and substrates by normalizing values to a coverage fraction of 30% [15]. The approach assumes a critical island size of one atom, negligible desorption, and isotropic two-dimensional diffusion. The normalized nucleation density, $N_{30\%}$, is given by

$$N_{30\%} = \sqrt[3]{\frac{3\theta_{30\%}^2}{t_{30\%}D_{30\%}}} = N \cdot \sqrt[3]{\frac{0.3}{\theta \cdot a_{\text{Bi}_2\text{Te}_3}^2 \cdot \sqrt{3}/2}}, \quad (1)$$

where N is the nucleation density, θ is the surface coverage, t is the growth time, D is the diffusion

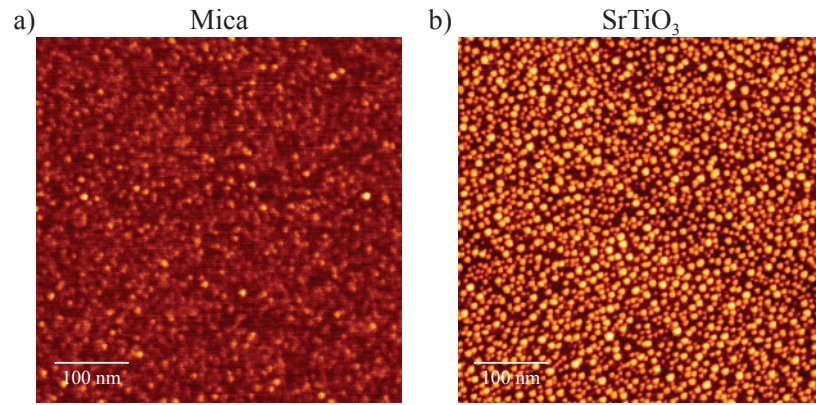


Figure 4: 500×500 nm AFM scans of 1-pulse films grown on mica (a) and SrTiO₃ (b) substrates. The background level is scaled to highlight the bright-colored nucleation sites at the surface.

Table 1: Nucleation density N , thickness h , coverage fraction φ , and normalized nucleation density $N_{30\%}$ of the one-pulse films

1 pulse	N (cm ⁻²)	h (nm)	φ (% area)	$N_{30\%}$ (cm ⁻²)
Mica	5×10^{11}	1	25	7×10^{11}
SrTiO ₃	9×10^{11}	3	56	5×10^{11}

constant, $a_{\text{Bi}_2\text{Te}_3}$ is the in-plane lattice parameter of Bi₂Te₃, and the subscript 30% denotes normalization to 30% coverage [15]. This expression can be reformulated in terms of quantities directly obtained from AFM measurements as

$$N_{30\%} = N \cdot \sqrt[3]{\frac{0.3}{\varphi} \cdot \frac{c_{\text{Bi}_2\text{Te}_3}}{3h}}, \quad (2)$$

where $c_{\text{Bi}_2\text{Te}_3}$ is the out-of-plane lattice parameter of the Bi₂Te₃ unit cell, φ is the coverage fraction, and h is the film thickness [29]. The parameters extracted from the AFM analysis are summarized in Table 1.

Figure 5(a) presents the resulting $N_{30\%}$ values for the one-pulse films on mica and SrTiO₃, together with the literature ranges for other growth techniques compiled in [29]. The calculated normalized nucleation densities are 5×10^{11} nuclei per cm² for SrTiO₃ and 7×10^{11} nuclei per cm² for mica. These values fall within the range typically reported for qvdW epitaxial growth by molecular beam epitaxy (MBE), while exceeding most reported values for purely vdW epitaxy across different deposition techniques. The relatively high nucleation densities observed for PLD are consistent with its supersaturated growth environment and comparatively low growth temperature. In the present study, Bi₂Te₃ growth is carried out at 220 °C, which is lower than temperatures typically employed by MBE or vapor-phase techniques and therefore limits adatom diffusion.

Using the measured surface coverage θ , the growth rate of the films deposited with 10, 25, and 50 pulses can also be estimated. The resulting values are summarized in Figure 5(b). A clear substrate-dependent trend emerges. On mica, the growth rate is initially lower, reflecting the reduced adsorption probability of the vdW surface. As the Bi₂Te₃ film begins to cover the substrate, the growth rate increases as incoming species increasingly interact with previously deposited Bi₂Te₃. In contrast, films grown on SrTiO₃ exhibit the opposite behavior: the initial growth rate is relatively high but decreases with increasing thickness as the influence of the substrate surface diminishes and adatom interactions become dominated by the growing film itself. At larger thicknesses the growth rates across different substrates converge, as also observed for films grown on Si₃N₄. The films deposited on BaF₂ constitute an outlier in this analysis, showing an apparent stagnation of growth relative to the other substrates, and are therefore excluded from further discussion.

Overall, the results indicate that Bi₂Te₃ nucleation densities during PLD are comparable to the observed for MBE growth, suggesting that nucleation is primarily determined by deposition conditions rather than the epitaxial regime alone. However, the substrate strongly affects the

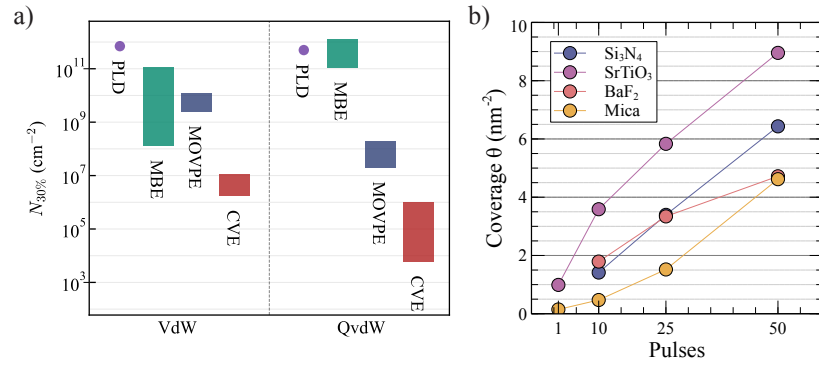


Figure 5: a) Comparison of normalized nucleation density between different growth techniques for van der Waals epitaxy and quasi van der Waals epitaxy. The ranges for MBE, MOVPE, and CVE are taken from [29], while the PLD values are calculated based on the 1-pulse samples. b) Calculated coverage θ values for all samples discussed.

Table 2: Electronic transport properties at 5K of Bi₂Te₃ deposited with 50 pulses on selected substrates. Table includes resistivity, conductivity, carrier density and mobility

	ρ (Ω m)	σ (S m ⁻¹)	n_{3D} (cm ⁻³)	μ (cm ² /Vs)
(001)Mica	$1.693 \cdot 10^{-5}$	$5.908 \cdot 10^4$	$4.402 \cdot 10^{19}$	83.76
(111)BaF ₂	$2.428 \cdot 10^{-5}$	$4.118 \cdot 10^4$	$1.184 \cdot 10^{20}$	21.70
(111)SrTiO ₃	$1.520 \cdot 10^{-5}$	$6.579 \cdot 10^4$	$1.540 \cdot 10^{20}$	26.66
Si ₃ N ₄	$1.720 \cdot 10^{-4}$	$5.813 \cdot 10^3$	$1.021 \cdot 10^{20}$	3.55

subsequent growth kinetics. The higher nucleation density observed on SrTiO₃ does not necessarily promote two-dimensional growth. Instead, the reduced diffusion length leads to rapid nucleation of many small islands, which subsequently grow preferentially out-of-plane once quintuple-layer nuclei are established. In contrast, the weaker adsorption on mica allows adatoms to diffuse over longer distances, resulting in fewer nuclei and more pronounced lateral island expansion. As growth proceeds and grains coalesce, the morphology of films on both substrates converges toward faceted domains with three-fold symmetry and well-defined QL steps.

3.3 Electronic transport

To investigate how structural and point defects influence the functional properties of the films, their electronic transport was characterized using van der Pauw measurements. Table 2 summarizes the transport parameters measured at 5K for Bi₂Te₃ films deposited with 50 laser pulses on the different substrates. All samples exhibit n-type conduction, indicating that the Fermi level lies within the conduction band. This behavior is consistent with slight Te deficiency, where tellurium vacancies act as donor-like defects and dominate the bulk charge transport.

Hall measurements reveal relatively high carrier concentrations in the range of 10¹⁹ to 10²⁰ cm⁻³, placing all films firmly within the bulk-conducting regime. Under these conditions, topological surface states are unlikely to dominate total conductance, although they may still dominate the phase-coherent component of the transport [30]. The measured mobility and resistivity values fall within the range typically reported for Bi₂Te₃ films grown by PLD and measured in the van der Pauw geometry [13]. However, compared to mobility values extracted from Shubnikov–de Haas measurements, the values observed here are relatively low, suggesting substantial carrier scattering in all films [31].

Clear substrate-dependent trends are observed when comparing the films. The film grown on mica exhibits the lowest resistivity (1.693×10^{-5} Ω m), the highest mobility (83.76 cm²/Vs), and the lowest carrier density 4.4×10^{19} cm⁻³. These values are generally considered favorable for accessing topological transport in Bi₂Te₃. Films grown on SrTiO₃ and BaF₂ display similar resistivity values of 1.5×10^{-5} Ω m and 2.4×10^{-5} Ω m, but substantially reduced mobility of 21.7 cm²/Vs and 16.7 cm²/Vs, respectively, indicating increased carrier scattering. The film deposited on Si₃N₄ exhibits the most degraded transport performance, with both resistivity and mobility differing by approximately an order of magnitude from those measured for the mica sample. This strongly suggests that structural disorder and porosity dominate the transport behavior and lead to

defect-induced scattering.

The observed mobility trends correlate well with the structural characterization presented in the previous sections. Films grown on mica exhibit the most ordered morphology with large, well-coalesced terraces and minimal porosity, which reduces scattering at grain boundaries. In contrast, the films grown on Si_3N_4 display the most disordered morphology, characterized by rough surfaces and a porous island network that significantly suppresses carrier mobility. Films grown on SrTiO_3 and BaF_2 exhibit intermediate mobilities, consistent with their intermediate topographical quality roughness associated with the step-terrace structure. These results suggest that grain boundaries and structural disorder play a dominant role in limiting carrier mobility.

Carrier density follows a different trend. The highest carrier concentration is observed for the film grown on SrTiO_3 , reaching $1.54 \times 10^{20} \text{ cm}^{-3}$, while the films on BaF_2 and Si_3N_4 exhibit similar values near $1.2 \times 10^{20} \text{ cm}^{-3}$ and $1.0 \times 10^{20} \text{ cm}^{-3}$, respectively. The increased carrier density in the SrTiO_3 film may be related to increased point-defect formation during the earliest stages of growth. This interpretation is consistent with the Raman analysis of the 10-pulse films, which indicated deviations from the ideal stoichiometry on this substrate.

While the Hall measurements indicate substantial bulk conduction, magnetotransport measurements provide a sensitive probe of the phase-coherent contribution to the transport. In particular, weak anti-localization arises from quantum interference effects in systems with strong spin-orbit coupling. In such systems, time-reversed electron path interfere destructively, suppressing backscattering and producing a characteristic cusp in the magnetoresistance near zero magnetic field [32]. WAL is frequently observed in topological insulators where spin-orbit coupling is strong and phase coherence can persist over relatively long length scales [33].

In two-dimensional systems the WAL correction to the classical Drude conductivity is described by the Hikami–Larkin–Nagaoka (HLN) model:

$$\Delta\sigma(B) = -\alpha \frac{e^2}{2\pi^2\hbar} \left[\psi \left(\frac{1}{2} + \frac{B_\varphi}{B} \right) - \ln \left(\frac{B_\varphi}{B} \right) \right], \quad (3)$$

where $\Delta\sigma(B)$ is the change in conductivity as a function of magnetic field B , α is a dimensionless prefactor related to the number of coherent conduction channels, ψ is the digamma function [34], and B_φ is the characteristic dephasing field [35]. The dephasing field is related to the phase-coherence length l_φ through

$$B_\varphi = \frac{\hbar}{4el_\varphi^2}. \quad (4)$$

Since the HLN model is formulated in terms of magnetoconductivity, the experimentally measured resistivity $\rho(B)$ is converted to conductivity using the approximate film thickness t according to

$$\sigma(B) = \frac{t}{\rho(B)}. \quad (5)$$

The conductivity correction used for fitting is then

$$\Delta\sigma(B) = \sigma(B) - \sigma(0). \quad (6)$$

Magnetoresistance measurements were performed on the films grown on mica and SrTiO_3 . Both samples exhibit pronounced WAL cusps at low magnetic fields, characteristic of strong spin–orbit coupling. Figure 6(a) shows the normalized magnetoresistance for the mica sample (data for SrTiO_3 are shown in the Supporting Information). The WAL feature gradually weakens with increasing temperature. The extracted HLN parameters for both films are summarized in Figure 6(b,c), which shows the temperature dependence of the prefactor α and the phase-coherence length (l_ϕ).

For a single two-dimensional conduction channel with strong spin-orbit coupling the HLN model predicts $\alpha = -\frac{1}{2}$. Additional coherent channels increase the magnitude of α . Contributions from bulk conductivity or disorder-induced electron–electron interactions cause the prefactor to deviate toward positive values [36]. For the mica sample, the prefactor remains close to $\alpha \approx -1$ across the entire temperature range. This value is often associated with two coherent and decoupled topological surface states [37, 38]. However, given the relatively high carrier density of

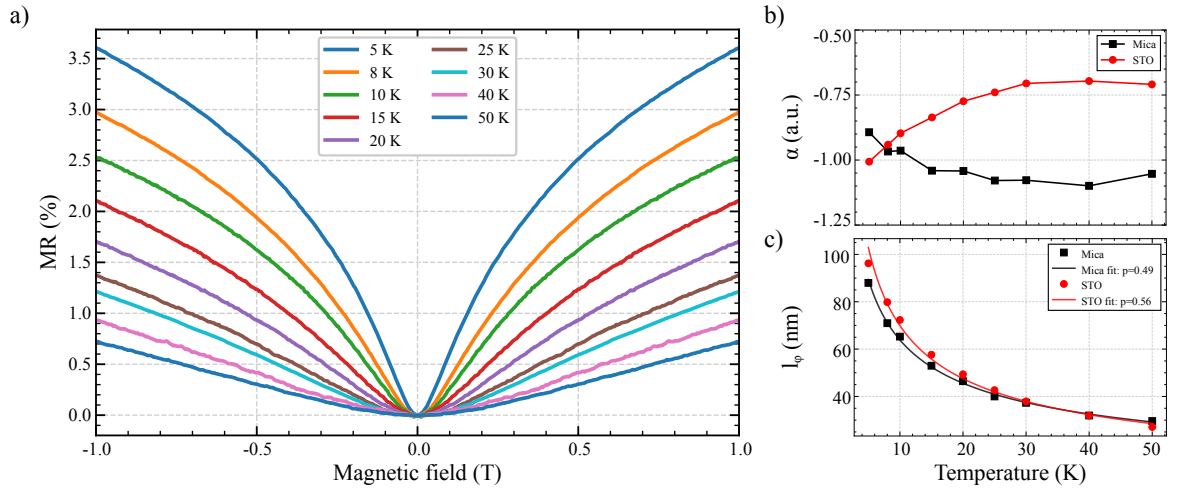


Figure 6: a) Magnetoresistance (MR%) of the Bi₂Te₃ film grown on mica showing clear WAL cusps that weaken with increasing temperature. b) HLN prefactor α for the mica and SrTiO₃ films. c) Phase-coherence length l_ϕ with power-law fits $l_\phi \propto T^{-p/2}$.

$n_{3D} = 4.4 \cdot 10^{19}$, a coherent bulk contribution is also expected [30]. In this case the observed $\alpha \approx -1$ likely reflects the combined contribution of a partially coherent bulk channel and a surface-derived channel, rather than two isolated surface states [39].

The film grown on SrTiO₃ exhibits a similar low-temperature value of $\alpha \approx -1$ at 5 K, but the prefactor gradually approaches $\alpha \approx -0.7$ as the temperature increases toward 30 K to 50 K. This behavior suggests that the surface contribution gradually loses phase coherence with increasing temperature, while the bulk channel remains relatively robust, consistent with previous observations in topological materials [32].

The temperature dependence of the phase-coherence length further clarifies the dominant dephasing mechanism [40]. For both samples the phase-coherence length follows a power-law dependence [41] of the form

$$l_\phi \propto T^{-p/2}. \quad (7)$$

Fitting the experimental data yields $p = 0.49$ for the mica film and $p = 0.56$ for the SrTiO₃ film, values characteristic of electron-electron interaction dominated dephasing in two-dimensional diffusive systems [42]. This behavior is consistent with a significant contribution of two-dimensional conduction channels to the phase-coherent transport.

The combined structural and electronic measurements reveal a clear hierarchy of mechanisms that govern the transport properties of ultrathin Bi₂Te₃ films. Substrate roughness first determines the effective diffusion landscape for incoming adatoms, thereby controlling nucleation density and island coalescence during the earliest stages of growth. These nucleation conditions subsequently determine grain size, terrace formation, and structural coherence of the films. Structural coherence primarily governs electron mobility through scattering at grain boundaries and morphological disorder. In parallel, substrate surface chemistry influences adsorption strength and early growth stoichiometry, which affects the formation of point defects that control the carrier density. Within this framework, atomically flat substrates such as mica promote extended adatom diffusion, lower nucleation density, and terrace-forming growth, resulting in higher mobilities and lower carrier concentrations. In contrast, substrates with higher surface reactivity or roughness increase nucleation density and defect formation, which suppress mobility and increase bulk carrier density. Notably, these results demonstrate that substrate roughness and substrate-dependent growth kinetics can dominate over lattice mismatch in determining the structural and electronic quality of PLD-grown Bi₂Te₃ films.

4 Conclusion

We systematically investigated the early-stage growth and electronic transport of ultrathin Bi₂Te₃ films deposited by pulsed laser deposition on substrates spanning distinct epitaxial regimes. While phase-pure, *c*-axis-oriented Bi₂Te₃ films were obtained on all substrates, the surface morphology

and growth pathways varied significantly. Atomically flat mica and step-terraced SrTiO₃ promote layered growth with well-defined quintuple-layer terraces, whereas films grown on BaF₂ and amorphous Si₃N₄ exhibit more irregular, island-structured morphologies. These differences correlate primarily with substrate roughness rather than nominal lattice mismatch.

Analysis of the earliest growth stages reveals substrate-dependent kinetic pathways. On mica, weak van der Waals interactions reduce adatom adsorption and favor the formation of single-quintuple-layer nuclei that expand predominantly in-plane. In contrast, the more reactive SrTiO₃ surface enhances adsorption, leading to higher nucleation densities and the formation of multi-QL nuclei that promote faster out-of-plane growth. Comparison with literature values shows that the normalized nucleation densities obtained by PLD are comparable to those reported for molecular beam epitaxy.

Transport measurements reveal n-type conduction across all samples with carrier densities in the range of 10¹⁹–10²⁰ cm⁻³, consistent with defect-induced doping dominated by tellurium vacancies. Electron mobility correlates strongly with structural coherence: films exhibiting terrace-forming growth on smooth substrates show higher mobilities, whereas rough or porous morphologies suppress mobility through enhanced scattering at grain boundaries and structural disorder. Magnetotransport measurements reveal clear weak anti-localization signatures in the films grown on mica and SrTiO₃, indicating the presence of phase-coherent conduction channels associated with strong spin–orbit coupling. Temperature-dependent measurements further suggest that surface-state contributions remain observable up to 50 K for the mica films, while they are increasingly masked by bulk conduction in the SrTiO₃ samples due to their higher carrier densities.

Taken together, the structural and electronic measurements reveal a hierarchy of mechanisms linking substrate properties to electronic transport in ultrathin Bi₂Te₃. Substrate roughness and surface chemistry determine adatom diffusion and nucleation density during the earliest stages of growth, which subsequently control grain size, terrace formation, and defect density. These structural characteristics ultimately govern carrier mobility and bulk carrier concentration. The results demonstrate that substrate-controlled growth kinetics—particularly surface roughness—can dominate over lattice matching in determining the structural and electronic quality of PLD-grown Bi₂Te₃ films. By identifying nucleation density and substrate morphology as key parameters, this work provides practical design guidelines for engineering Bi₂Te₃ heterostructures with reduced defect densities and enhanced topological surface transport.

Funding

This project was supported by the Research Council of Norway under Project Number 325063. The Research Council of Norway is acknowledged for the support to the Norwegian Micro- and Nano-Fabrication Facility, NorFab, project number 295864.

Author contributions

D.B.: Conceptualization, data curation, formal analysis, investigation, methodology. S.R.H.: Data curation, formal analysis, investigation. E.Y.T.: Data curation, formal analysis, investigation. J.A.A.: Data curation, formal analysis, investigation. I.G.H.: Conceptualization, funding acquisition, methodology, project administration.

Data availability

All data that support the findings of this study are included within the article (and any supplementary files).

Supplementary data

The following files are available free of charge. Supporting information containing: Raman intensity ratios, diffractograms and AFM scans of 10- and 25-pulse samples, SEM images of 10-, 25-, and 50-pulse samples, magnetoresistance of the film grown on SrTiO₃.

References

- [1] Haijun Zhang, Chao-Xing Liu, Xiao-Liang Qi, Xi Dai, Zhanxi Fang, and Shou-Cheng Zhang. Topological insulators in Bi₂Se₃, Bi₂Te₃ and Sb₂Te₃ with a single dirac cone on the surface. *Nature Physics*, 5:438–442, 05 2009.

- [2] Kajetan Fijalkowski, Nan Liu, Pankaj Mandal, S. Schreyeck, Karl Brunner, Charles Gould, and Laurens Molenkamp. Quantum anomalous hall edge channels survive up to the curie temperature. *Nature Communications*, 12, 09 2021.
- [3] Yi-Fan Zhao, Ruoxi Zhang, Zi-Ting Sun, Ling-Jie Zhou, Deyi Zhuo, Zi-Jie Yan, Hemian Yi, Ke Wang, Moses H. W. Chan, Chao-Xing Liu, K. T. Law, and Cui-Zu Chang. 3D quantum anomalous hall effect in magnetic topological insulator trilayers of hundred-nanometer thickness. *Advanced Materials*, 36(13):2310249, 2024.
- [4] Z. Aabdin, N. Peranio, M. Winkler, D. Bessas, J. König, R. P. Hermann, H. Böttner, and O. Eibl. Sb_2Te_3 and Bi_2Te_3 thin films grown by room-temperature mbe. *Journal of Electronic Materials*, 41:1493–1497, 6 2012.
- [5] J. Krumrain, G. Mussler, S. Borisova, T. Stoica, L. Plucinski, C. M. Schneider, and D. Grützmacher. Mbe growth optimization of topological insulator Bi_2Te_3 films. *Journal of Crystal Growth*, 324:115–118, 6 2011.
- [6] A. Bailini, F. Donati, M. Zamboni, V. Russo, M. Passoni, C. S. Casari, A. Li Bassi, and C. E. Bottani. Pulsed laser deposition of Bi_2Te_3 thermoelectric films. *Applied Surface Science*, 254:1249–1254, 12 2007.
- [7] Zhaoliang Liao, Matthew Brahlek, Jong Mok Ok, Lauren Nuckols, Yogesh Sharma, Qiyang Lu, Yanwen Zhang, and Ho Nyung Lee. Pulsed-laser epitaxy of topological insulator Bi_2Te_3 thin films. *APL Materials*, 7, 4 2019.
- [8] Lalit Pandey, Sajid Husain, Vineet Barwal, Soumyarup Hait, Nanhe Kumar Gupta, Vireshwar Mishra, Nakul Kumar, Nikita Sharma, Dinesh Dixit, Veer Singh, and Sujeet Chaudhary. Topological transport properties of highly oriented Bi_2Te_3 thin film deposited by sputtering. *Journal of Physics Condensed Matter*, 35, 9 2023.
- [9] Hongjing Shang, Fazhu Ding, Guicun Li, Li Wang, Fei Qu, Huiliang Zhang, Zebin Dong, He Zhang, Zhaoshun Gao, Weiwei Zhou, and Hongwei Gu. High performance co-sputtered Bi_2Te_3 thin films with preferred orientation induced by MgO substrates. *Journal of Alloys and Compounds*, 726:532–537, 2017.
- [10] Omar Concepción, Miguel Galván-Arellano, Vicente Torres-Costa, Aurelio Climent-Font, Daniel Bahena, Miguel Manso Silván, Arturo Escobosa, and Osvaldo De Melo. Controlling the epitaxial growth of Bi_2Te_3 , BiTe , and Bi_4Te_3 pure phases by physical vapor transport. *Inorganic Chemistry*, 57:10090–10099, 8 2018.
- [11] Qile Li, Iolanda Di Bernardo, Johnathon Maniatis, Daniel McEwen, Amelia Dominguez-Celorrío, Mohammad T. H. Bhuiyan, Mengting Zhao, Anton Tadich, Liam Watson, Benjamin Lowe, Thi-Hai-Yen Vu, Chi Xuan Trang, Jinwoong Hwang, Sung-Kwan Mo, Michael S. Fuhrer, and Mark T. Edmonds. Imaging the breakdown and restoration of topological protection in magnetic topological insulator MnBi_2Te_4 . *Advanced Materials*, 36(24):2312004, 2024.
- [12] M. Mogi, Mayuka Kawamura, R. Yoshimi, A. Tsukazaki, Y. Kozuka, N. Shirakawa, K. Takahashi, M. Kawasaki, and Y. Tokura. A magnetic heterostructure of topological insulators as a candidate for an axion insulator. *Nature Materials*, 16, 02 2017.
- [13] Xinfeng Tang, Ziwei Li, Wei Liu, Qingjie Zhang, and Ctirad Uher. A comprehensive review on Bi_2Te_3 -based thin films: thermoelectrics and beyond. *Interdisciplinary Materials*, 1:88–115, 1 2022.
- [14] Dominik Kriegner, Petr Hrcuba, Jozef Veselý, Andreas Lesnik, Guenther Bauer, Gunther Springholz, and Václav Holý. Twin domain imaging in topological insulator Bi_2Te_3 and Bi_2Se_3 epitaxial thin films by scanning x-ray nanobeam microscopy and electron backscatter diffraction. *Journal of Applied Crystallography*, 50:369–377, 2017.
- [15] Wouter Mortelmans, Stefan De Gendt, Marc Heyns, and Clement Merckling. Epitaxy of 2d chalcogenides: aspects and consequences of weak van der waals coupling. *Applied Materials Today*, 22:100975, 2021.
- [16] Lee A. Walsh and Christopher L. Hinkle. Van der waals epitaxy: 2d materials and topological insulators, 12 2017.

- [17] Asteriona-Maria Netsou, Dmitry Muzychenko, Heleen Dausy, Taishi Chen, Fengqi Song, Koen Schouteden, Margriet Bael, and Chris Van Haesendonck. Identifying native point defects in the topological insulator Bi_2Te_3 . *ACS Nano*, 14:13172–13179, 10 2020.
- [18] Vanda M. Pereira, Chi Nan Wu, Katharina Höfer, Arnold Choa, Cariad A. Knight, Jesse Swanson, Christoph Becker, Alexander C. Komarek, A. Diana Rata, Sahana Rößler, Steffen Wirth, Mengxin Guo, Minghui Hong, Jueina Kwo, Liu Hao Tjeng, and Simone G. Altendorf. Challenges of topological insulator research: Bi_2Te_3 thin films and magnetic heterostructures. *Physica Status Solidi (B) Basic Research*, 258, 1 2021.
- [19] Nabakumar Rana, Pintu Singha, Suchandra Mukherjee, Subarna Das, Gangadhar Das, Apurba Kanti Deb, Sujay Chakravarty, S. Bandyopadhyay, and Aritra Banerjee. Origin of linear magnetoresistance in Bi_2Te_3 topological insulator: role of surface state and defects. *Physica B: Condensed Matter*, 679:415801, 2024.
- [20] David Nečas and Petr Klapetek. Gwyddion: an open-source software for SPM data analysis. *Central European Journal of Physics*, 10:181–188, 2012.
- [21] Guillaume Vignaud and Alain Gibaud. REFLEX: a program for the analysis of specular X-ray and neutron reflectivity data. *Journal of Applied Crystallography*, 52(1):201–213, Feb 2019.
- [22] V. Russo, A. Bailini, M. Zamboni, M. Passoni, C. Conti, C. S. Casari, A. Li Bassi, and C. E. Bottani. Raman spectroscopy of bi-te thin films. In *Journal of Raman Spectroscopy*, volume 39, pages 205–210. John Wiley and Sons Ltd, 2008.
- [23] P.I. Kuznetsov, V.O. Yapaskurt, B.S. Shchamkhalova, V.D. Shcherbakov, G.G. Yakushcheva, V.A. Luzanov, and V.A. Jitov. Growth of Bi_2Te_3 films and other phases of bi-te system by mope. *Journal of Crystal Growth*, 455:122–128, 2016.
- [24] Hao Xu, Yuxin Song, Wenwu Pan, Qimiao Chen, Xiaoyan Wu, Pengfei Lu, Qian Gong, and Shumin Wang. Vibrational properties of epitaxial Bi_4Te_3 films as studied by raman spectroscopy. *AIP Advances*, 5(8):087103, 08 2015.
- [25] Leonarde N. Rodrigues, C. I. L. de Araujo, S. L. A. Mello, J. Laverock, Jakson M. Fonseca, W. Schwarzacher, Wesley F. Inoch, and Sukarno O. Ferreira. Growth of Bi_2Te_3 topological insulator ultra-thin layers via molecular beam epitaxy on GaAs (100). *Journal of Applied Physics*, 134(8):085301, 08 2023.
- [26] K. M.F. Shahil, M. Z. Hossain, D. Teweldebrhan, and A. A. Balandin. Crystal symmetry breaking in few-quintuple Bi_2Te_3 films: applications in nanometrology of topological insulators. *Applied Physics Letters*, 96:153103, 4 2010.
- [27] Y. Liu, M. Weinert, and L. Li. Spiral growth without dislocations: Molecular beam epitaxy of the topological insulator Bi_2Se_3 on epitaxial graphene/SiC(0001). *Physical Review Letters*, 108, 3 2012.
- [28] Marhoun Ferhat, Jean Claude Tedenac, and Jiro Nagao. Mechanisms of spiral growth in Bi_2Te_3 thin films grown by the hot-wall-epitaxy technique. *Journal of Crystal Growth*, 218(2):250–258, 2000.
- [29] Wouter Mortelmans, Ankit Nalin Mehta, Yashwanth Balaji, Stefanie Sergeant, Ruishen Meng, Michel Houssa, Stefan De Gendt, Marc Heyns, and Clement Merckling. On the van der waals epitaxy of homo-/heterostructures of transition metal dichalcogenides. *ACS Applied Materials & Interfaces*, 12(24):27508–27517, Jun 2020.
- [30] James G Analytis, Jiun-Haw Chu, Yulin Chen, Felipe Corredor, Ross D McDonald, ZX Shen, and Ian R Fisher. Bulk fermi surface coexistence with dirac surface state in Bi_2Se_3 : a comparison of photoemission and shubnikov-de haas measurements. *Physical Review B—Condensed Matter and Materials Physics*, 81(20):205407, 2010.
- [31] Prosper Ngabonziza. Quantum transport and potential of topological states for thermoelectricity in Bi_2Te_3 thin films. *Nanotechnology*, 33(19):192001, 2022.
- [32] Hai-Zhou Lu and Shun-Qing Shen. Weak localization and weak anti-localization in topological insulators. In *Spintronics VII*, volume 9167, pages 263–273. SPIE, 2014.

- [33] Hong-Tao He, Gan Wang, Tao Zhang, Iam-Keong Sou, George K L Wong, Jian-Nong Wang, Hai-Zhou Lu, Shun-Qing Shen, and Fu-Chun Zhang. Impurity effect on weak antilocalization in the topological insulator Bi_2Te_3 . *Physical review letters*, 106(16):166805, 2011.
- [34] Milton Abramowitz and Irene A Stegun. Handbook of mathematical functions with formulas, graphs, and mathematical tables. *National Bureau of Standards Applied Mathematics Series*, e, 55:953, 1965.
- [35] Shinobu Hikami, Anatoly I Larkin, and Yosuke Nagaoka. Spin-orbit interaction and magnetoresistance in the two dimensional random system. *Progress of Theoretical Physics*, 63(2):707–710, 1980.
- [36] Shao-Pin Chiu and Juhn-Jong Lin. Weak antilocalization in topological insulator Bi_2Te_3 microflakes. *Physical Review B—Condensed Matter and Materials Physics*, 87(3):035122, 2013.
- [37] Hadar Steinberg, J-B Laloë, Valla Fatemi, Jagadeesh S Moodera, and Pablo Jarillo-Herrero. Electrically tunable surface-to-bulk coherent coupling in topological insulator thin films. *Physical Review B—Condensed Matter and Materials Physics*, 84(23):233101, 2011.
- [38] J Chen, HJ Qin, F Yang, J Liu, T Guan, FM Qu, GH Zhang, JR Shi, XC Xie, CL Yang, et al. Gate-voltage control of chemical potential and weak antilocalization in Bi_2Se_3 . *Physical Review Letters*, 105(17):176602, 2010.
- [39] A. A. Taskin, Satoshi Sasaki, Kouji Segawa, and Yoichi Ando. Manifestation of topological protection in transport properties of epitaxial Bi_2Se_3 thin films. *Phys. Rev. Lett.*, 109:066803, Aug 2012.
- [40] Thomas Barthel and Ulrich Schollwöck. Dephasing and the steady state in quantum many-particle systems. *Physical review letters*, 100(10):100601, 2008.
- [41] Juhn-Jong Lin and JP Bird. Recent experimental studies of electron dephasing in metal and semiconductor mesoscopic structures. *Journal of Physics: Condensed Matter*, 14(18):R501–R596, 2002.
- [42] Alex L Efros and Michael Pollak. *Electron-electron interactions in disordered systems*, volume 10. Elsevier, 2012.

Supporting Information: Substrate-controlled nucleation and growth kinetics in ultrathin Bi_2Te_3 films

Damian Brzozowski¹, Sander R. Hønnås¹, Egil Y. Tokle¹, Jørgen A. Arnesen¹, and Ingrid G. Hallsteinsen¹

¹*Department of Materials Science and Engineering, Norwegian University of Science and Technology, Trondheim, Norway*

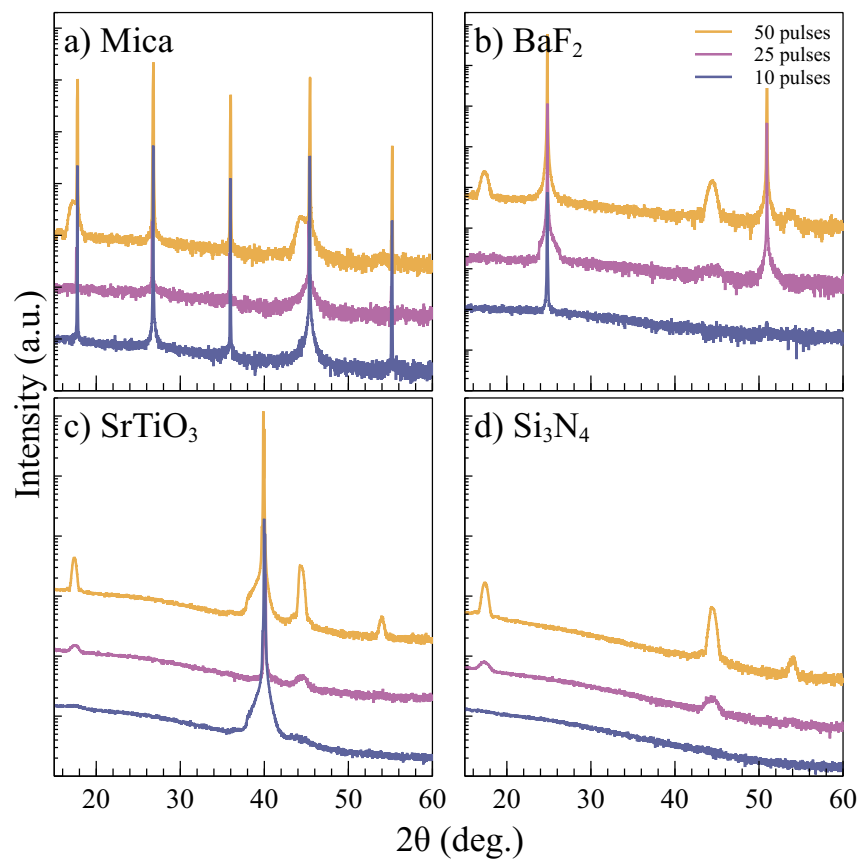


Figure 1: Widescan Bragg-Brentano diffractograms of deposited Bi_2Te_3 thin films.

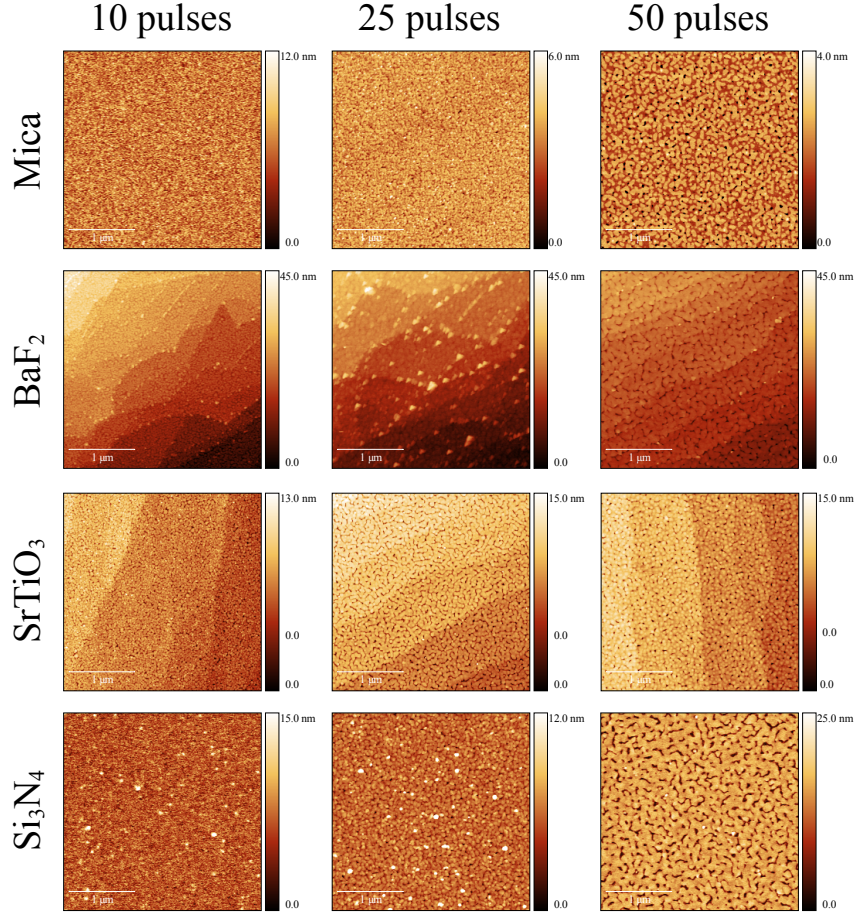


Figure 2: AFM scans of the 10-, 25- and 50-pulse Bi_2Te_3 thin films.

Table 1: Calculated ratio of E_g^2 to A_{1g}^2 Raman peaks of the 10-, 25-, and 50-pulse Bi_2Te_3 thin films

No. of pulses	Mica	BaF ₂	SrTiO ₃	Si ₃ N ₄
10	2.65	1.95	—	2.25
25	2.78	2.80	3.53	2.92
50	3.05	3.31	3.36	3.35

Table 2: The summary of topographical features of Bi_2Te_3 films across the selected numbers for laser pulses

No. of pulses	(001)Mica			(111)BaF ₂			(111)SrTiO ₃			Si ₃ N ₄		
	10	25	50	10	25	50	10	25	50	10	25	50
thickness (nm)	1	3	8	4	7	9	7	11	16	4	8	12
fraction coverage (%)	80	86	98	76	81	89	87	90	95	60	72	91
formula units per area (nm ⁻²)	5	15	46	18	33	47	36	58	90	14	34	64
roughness (nm)	1.3	0.5	0.7	1.5	1.8	2.1	1.1	1.7	1.3	1.6	1.1	3.4

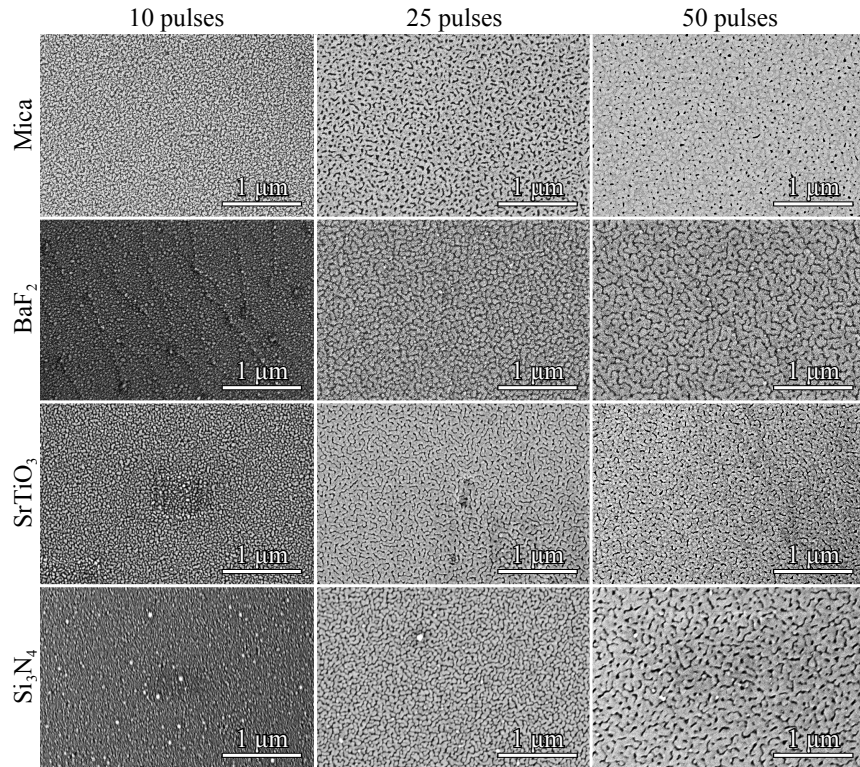


Figure 3: SEM images of the 10-, 25-, and 50-pulse Bi₂Te₃ thin films.

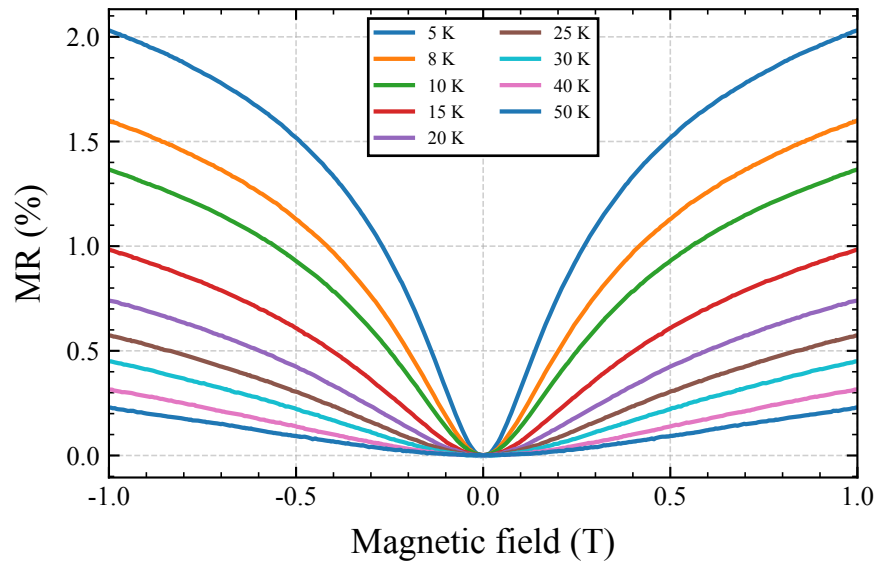


Figure 4: Magnetoresistivity of the Bi₂Te₃ thin film deposited on the SrTiO₃ substrate.